Journal of Sciences, Islamic Republic of Iran 22(3): 221-238 (2011) http://jsciences.ut.ac.ir
University of Tehran, ISSN 1016-1104

Application of Spectral Analysis in Mapping Hydrothermal Alteration of the Northwestern Part of the Kerman Cenozoic Magmatic Arc, Iran

M. Honarmand[1], H. Ranjbar[2,*] and J. Shahabpour[1]

[1]*Department of Geology, Faculty of sciences, Shahid Bahonar University of Kerman, Kerman, Islamic Republic of Iran*
[2]*Department of Mining Engineering, Faculty of engineering, Shahid Bahonar University of Kerman, kerman, Islamic Republic of Iran*

Received: 20 October 2010 / Revised: 13 September 2011 / Accepted: 12 November 2011

Abstract

The northwestern part of the Kerman Cenozoic magmatic arc (KCMA) contains many areas with porphyry copper mineralization. In this research, we used the advanced space-borne thermal emission and reflection radiometer (ASTER) and Enhanced Thematic Mapper plus (ETM^+) images of this region to map the distribution of hydrothermally altered rocks, based on their mineral assemblages. The spectral measurements based on the spectra of field samples and on ASTER and ETM^+ data, show dominantly Al-OH (sericite and clays) and FeO absorption features in the VNIR/SWIR spectral regions. Directed principal components analysis (DPCA), spectral angle mapper (SAM) and linear spectral unmixing (LSU) were performed on ASTER/ETM^+ images to map zones of hydrothermal alteration and iron oxide/hydroxide minerals. The individual principal components (PC) images generated by DPCA reveal the distribution of individual alteration minerals such as sericite, illite, kaolinite, chlorite, and epidote. The best results, in terms of mapping the distribution of alteration, were obtained using the SAM and LSU methods; but the LSU method produced a more accurate map. The altered zones were sampled and then subjected to X-ray diffraction (XRD), laboratory spectral and chemical analyses. Microscopic studies of the thin sections were also conducted. Field observations reveal that more than 90% of the known copper mineralized localities occur within the interpreted alteration areas.

Keywords: Porphyry copper; Hydrothermal alteration; DPCA; SAM; LSU

Introduction

The Urumieh-Dokhtar magmatic belt (UDMB) hosts porphyry copper deposits and is one of the main copper-bearing regions in the world, with great potential for Cenozoic porphyry copper mineralization (Fig. 1a).

* Corresponding author, Tel.: +98(913)1420464, Fax: +98(341)2121003, E-mail: h.ranjbar@mail.uk.ac.ir

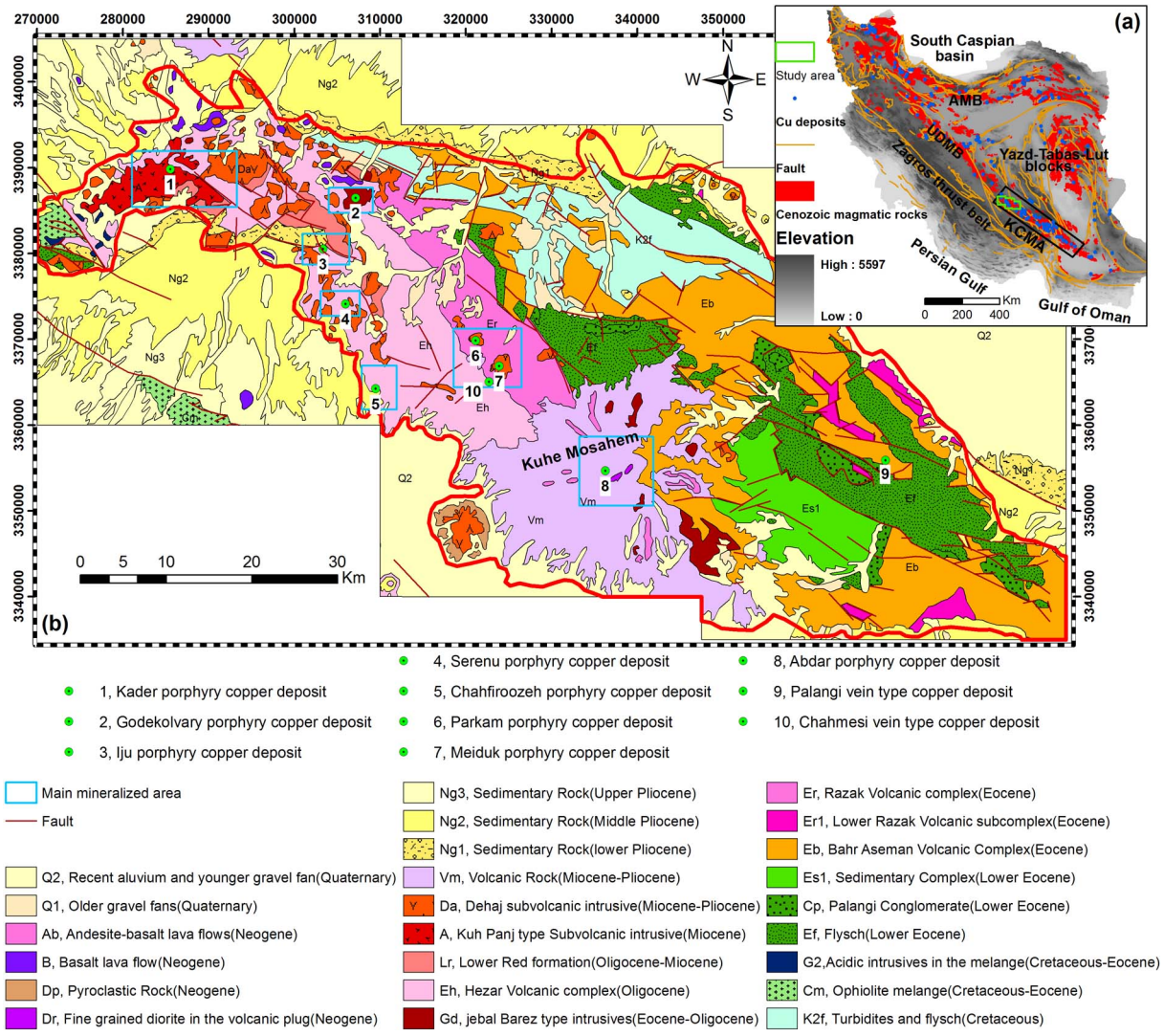

Figure 1. (a) Relief map showing the position of Cenozoic volcanic belts (compiled from Bazin and Hubner [3]; Shafiei et al. [51]). Abbreviations used: AMB, Alborz magmatic belt, UDMB, Urumieh-Dokhtar magmatic belt, KCMA, Kerman Cenozoic magmatic arc. (b) Simplified geological map of the study area (Adopted from Dimitrijevic [14]; Saric and Mijalkovic [50]). Locations of the copper deposits are shown. The red polygon outlines the KCMA (the outside of this boundary is masked).

Magmatic activity in this zone started in Eocene and reached a climax during the middle Eocene for volcanic rocks and during the Oligocene–Miocene for plutonic rocks, in many parts of Iran [2,6,51]. Magmatic activity and copper mineralization within the UDMB is generally associated with porphyry copper and skarn mineralization, including deposits such as Sar Cheshmeh [56,52,22], Sungun [23], Meiduk [20,6] and many other economic and sub-economic ore bodies [57].

The Kuhe Mosahem–Kuhe Madvar area, which is part of the Kerman Cenozoic magmatic arc (KCMA), is known for its porphyry copper mineralization. Figure 1b shows a simplified geological map of the study area. The oldest rocks are Cretaceous and Eocene flysch deposits in the north, and Cretaceous coloured mélanges in the south. The youngest features are Quaternary alluvial deposits and gravel fans. The Lower Eocene rocks are part of a volcanic complex (Bahr Aseman complex). The formation of this complex was followed by the development of volcanic complexes during the Eocene (Razak complex) and Oligocene (Hezar complex) [20]. The Oligocene–Miocene intrusive rocks were emplaced into the volcanic rocks as stocks and dykes. The volcanic complexes and intrusive rocks are

Table 1. Summary characteristics of the major copper deposits in the study area (modified after GSI [19]; NICICO.a [41]; NICICO.b [42])

	Deposit	Type of mineralization	Host rocks	Main ore minerals	Tonnage and grade
1	Kader	Porphyry	Diorite porphyry, Quartz diorite porphyry	Pyrite, Chalcopyrite, Chalcocite, Covellite	----------
2	Godekolvary	Porphyry	Diorite porphyry, Granodiorite, Andesite	Pyrite, Chalcopyrite	----------
3	Iju	Porphyry	Diorite porphyry, Quartz diorite porphyry	Pyrite, Chalcopyrite, Chalcocite	15.42 Mt, 0.59% Cu
4	Serenu	Porphyry	Diorite porphyry, Quartz diorite porphyry, Andesite	Pyrite, Chalcopyrite	----------
5	Chahfiroozeh	Porphyry	Granodiorite porphyry	Malachite, Azurite, Chrysocolla, Pyrite, Chalcopyrite	47.5 Mt, 0.63% Cu
6	Parkam	Porphyry	Diorite porphyry, Micro diorite porphyry	Pyrite, Chalcopyrite, Malachite	----------
7	Meiduk	Porphyry	Diorite porphyry	Pyrite, Chalcopyrite, Chalcocite, Malachite	144 Mt, 0.84% Cu
8	Abdar	Vein and Porphyry	Granodiorite porphyry, Dasite porphyry, Andesite and diorite	Pyrite, Chalcopyrite, Galena, Malachite	----------
9	Palangi	Impregnation	Andesite and pyroclastites	Chalcopyrite, Malachite, Azurite, Chalcocite, Bornite	0.224 Mt, 2.147% Cu
10	Chahmesi	Vein	Andesite, Diorite porphyry	Chalcopyrite, Chalcocite, Sphalerite, Malachite, Azurite, Galena	1.825 Mt, 1.06 %Cu

partly covered by Late Miocene–Pliocene volcanic and subvolcanic rocks of the Mosahem stratovolcanoes. The youngest intrusive phase in the area is Dehaj-type subvolcanic bodies, and the youngest volcanic rocks are Quaternary trachytes and dacites [14, 20].

The Kuhe Mosahem–Kuhe Madvar area contains several mineral deposits and many important mineral occurrences. Porphyry-type mineralization is dominant, mainly near Post-Eocene intrusive bodies in the Eocene volcano-sedimentary complex. The most important porphyry copper deposits in this area are those at Kader, Godekolvary, Iju, Serenu, Chahfiroozeh, Parkam, Meiduk, and Abdar. An impregnation deposit occurs at Palangi, and a polymtallic vein-type deposit occurs at Chahmesi [14] (Fig. 1b; Table 1). The porphyry copper deposits in this area are associated with well-developed zones of hydrothermal alteration, including phyllic, argillic, propylitic, silicification, and Jarosite zones.

Porphyry copper deposits have received considerable attention in the remote sensing community in terms of mineral exploration [eg., 34, 45, 24, 43, 27, 38, 54, 25]. Zones of hypogene hydrothermal alteration and weathering associated with porphyry copper deposits are large enough to be detected and mapped using multispectral remote sensing data. In porphyry systems, the potassic zone is located in the centre, progressing radially outward to the phyllic, argillic, and propylitic zones [37] (Fig. 2). The mineral assemblages associated with these alteration zones show spectral absorption features in the visible–near infrared (VNIR) and shortwave infrared (SWIR) wavelength regions [1]. Accordingly, multispectral images with sufficient spectral and spatial resolution can be used to map these hydrothermally altered zones.

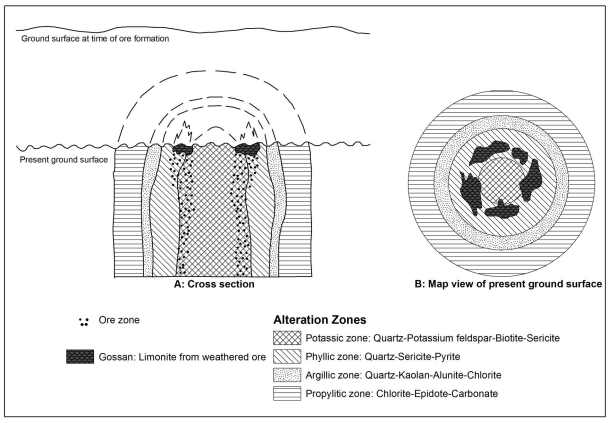

Figure 2. Model of hydrothermal alteration zones associated with porphyry copper deposit, which includes potassic, phyllic, argillic and propylitic alteration (Modified from Sabins [49]).

Table 2. Summary of performance characteristics for ASTER and ETM sensors (Summarized from Sabins [49]; Hubbard and Crowley [27]).

Multispectral sensor	Subsystem	Band number	Spectral range (μm)	Spatial Resolution (m)	Swath Width (Km)
ASTER	VNIR	1 (nadir)	0.52-0.60	15	60
		2 (nadir)	0.63-0.69		
		3 (nadir)	0.78-0.86		
		3 (backward)	0.78-0.86		
	SWIR	4	1.600-1.700	30	
		5	2.145-2.185		
		6	2.185-2.225		
		7	2.235-2.285		
		8	2.295-2.365		
		9	2.360-2.430		
	TIR	10	8.125-8.475	90	
		11	8.475-8.825		
		12	8.925-9.275		
		13	10.25-10.95		
		14	10.95-11.65		
ETM^+	VNIR	Panchromatic	0.520-0.900	15	185
		1	0.450-0.515	30	
		2	0.525-0.605		
		3	0.630-0.690		
		4	0.750-0.900		
	SWIR	5	1.550-1.750		
		7	2.090-2.350		
	TIR	6	10.40-12.50	60	

Table 2 lists the characteristics of the advanced spaceborne thermal emission and reflection radiometer (ASTER) and Enhanced Thematic Mapper plus (ETM^+). ASTER bands are more spectrally contiguous than the ETM^+ sensor, especially in the SWIR and TIR (thermal infrared) regions. Thus, the ASTER sensor can achieve greater accuracy in the spectral identification of rocks and minerals by using their absorption and reflection features in the SWIR region of the spectrum. The VNIR bands contain important information regarding absorption features related to transition metals (e.g., Fe^{2+}, Fe^{3+}) within Fe-oxide/hydroxide minerals. ETM^+ is able to map these minerals, because it has four spectral bands in the VNIR region.

Mars and Rowan [38] used remotely sensed ASTER data to map zones of alteration at a regional scale in the Iranian volcano-sedimentary belt, which includes the present study area. The authors applied multiple band ratios and calculated threshold values for mapping argillic and phyllic zones. Tangestani et al. [54] used ASTER data in an analysis of a small part of this area (the Meiduk and Abdar deposits) with the aim of delineating areas of alteration. The authors performed a principal component analysis (PCA) and used spectral angle mapper (SAM) to detect zones of alteration. Geological survey of Iran in a project so called "Urumieh Dokhtar belt exploration" explored the area using TM data [40].

The aims of the present study are to (1) perform directed principal component analysis (DPCA), apply spectral angle mapper (SAM) and linear spectral unmixing (LSU) to map zones of hydrothermal alteration around porphyry copper deposits using ASTER and ETM^+ data; (2) validate the results obtained using each method based on field data; and (3) determine which of the three methods performs best in mapping the distribution of alteration.

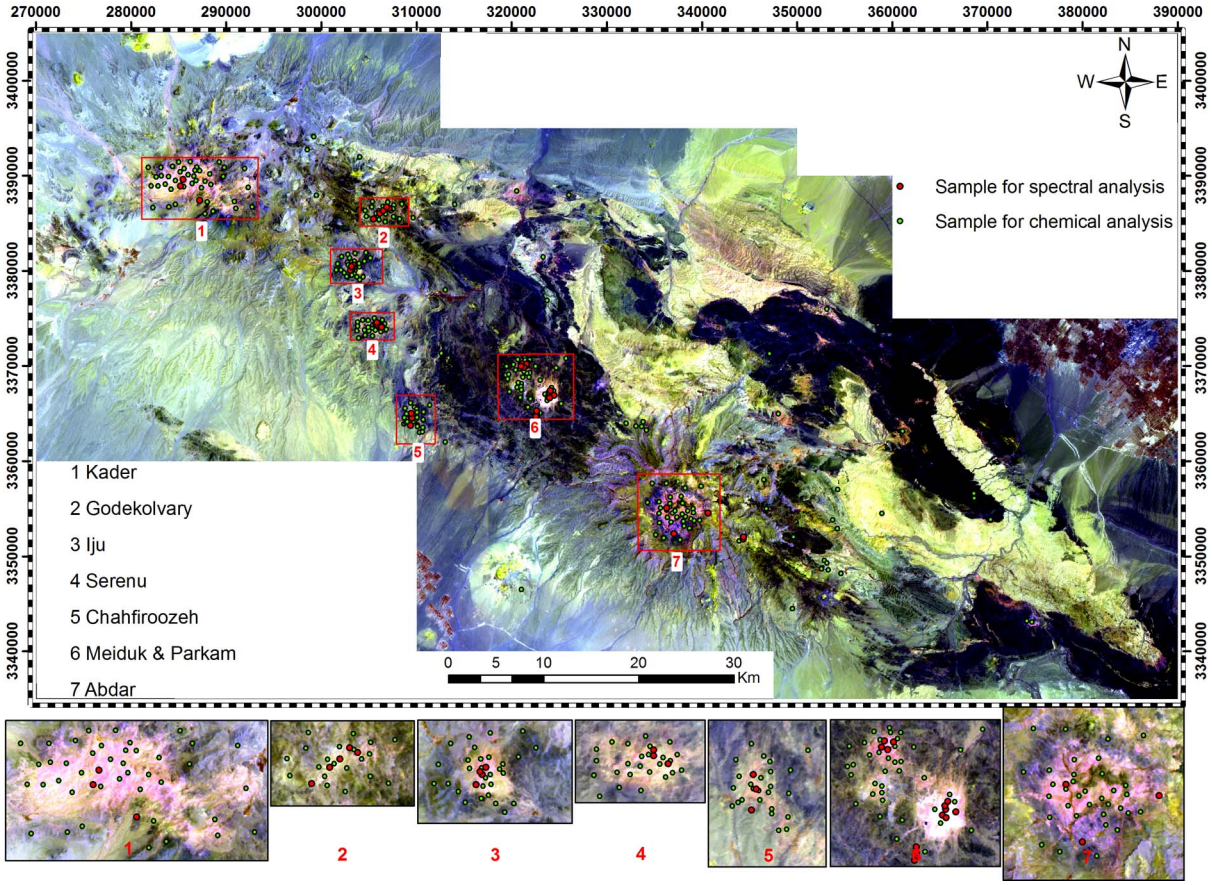

Figure 3. RGB colour composite of bands 4 (Red), 6 (Green) and 1 (Blue). The larger images of the mineralized areas are shown. The samples' locations are shown by black dots.

Materials and Methods

We analysed six individual ASTER scenes from cloud-free level-1B images (acquisition dates: 13 July 2003, 18 April 2001, 10 August 2001, and 25 July 2003). Crosstalk correction was applied on data acquired prior to 2001, using the crosstalk correction software (CCS) provided by the Earth remote sensing data centre (ERSDAC) [30]. This correction was performed to reduce the SWIR crosstalk effect, which is caused by the dispersion of incident light of the band 4 detector to other detectors in the SWIR region.

ASTER level-1B radiance images were converted to surface reflectance using fast line-of-sight atmospheric analysis of spectral hypercubes (FLAASH) software [39]. The images were pre-georeferenced to a UTM Zone 40 north projection with WGS-84 datum and once more orthorectified and reprojected using a digital elevation model (Shuttle Radar Terrain Mission with spatial resolution of 30 meters) and orthorectified Landsat ETM$^+$ imagery. The six scenes were clipped and combined to form a single image mosaic with an approximate area of 5787 km^2.

ETM$^+$ data, which were already in reflectance format (acquisition date: 31 July 2004), were orthorectified and reprojected using a digital elevation model. The ASTER (bands 3–9) and ETM$^+$ (bands 1–3) data were combined to form a single 10-band file for further analysis. To perform spectral analysis, the ETM$^+$, VNIR, and SWIR bands were atmospherically corrected using the internal average relative reflectance (IARR) method [32, 5]. In the IARR technique, the average scene spectrum is calculated and used as the reference spectrum, which is then divided by the spectrum at each pixel in the image.

As this work was mainly focused on mapping of hydrothermal alteration in the volcano-plutonic belt, the sedimentary rocks outside the volcanic and plutonic rocks, that do not have porphyry copper potential, were masked (see Fig. 1b).

Figure 3 shows a false-colour composite image

(ASTER bands R-G-B = 4-6-1) of the study area. At the bottom of the image, the major zones of porphyry-type copper mineralization are shown at a larger scale, revealing lithological variations. Hydroxyl-bearing minerals are shown by a magenta colour in the figure.

PCA, SAM and LSU methods were used to map alteration zones associated with porphyry copper mineralization. The results, obtained from each method, were assessed and compared based on analyses of selected sites as ground control points (Fig. 3), from where samples were collected and subjected to spectral measurements, X-ray diffraction (XRD) analysis, and the studies of thin sections under a microscope.

Spectral Characteristics of Alteration in Relation to ASTER and ETM$^+$ Data

For the present study area, the VNIR+SWIR spectral regions of ETM$^+$+ASTER data are expected to enable discrimination of the main alteration minerals. Hydrothermal alteration zones are widespread in this region. The main alteration minerals are muscovite (sericite), kaolinite, montmorillonite, chlorite, epidote, carbonates, silica and jarosite.

Analyses of field samples, including observations of thin sections, XRD analysis, and spectroradiometer measurements reveal that sericitization is the most intensive and widespread form of hydrothermal alteration in the study area. This type of alteration is usually directly associated with areas of copper mineralization. The sericite alteration is sometimes associated with argillization, silicification, and bleaching of the surrounding rocks. Argillization is also common, although not as intensive as the sericitization. Choloritization affects ferromagnesian minerals in all rock types of the propylitic zone. Epidotization and carbonitization are associated with chloritization, and jarosite occurs in surface outcrops of hydrothermally altered rocks near areas of copper mineralization (e.g., at Iju, Parkam). Jarosite veinlets cut through previously altered rocks and are usually accompanied by goethite and hematite.

Figure 4a shows the VNIR+SWIR reflectance spectra of important hydrothermal alteration minerals, and Figure 4b shows the secondary iron oxides/hydroxides bearing minerals of relevance to the present study. The hydrothermal alteration zones are characterised by mineral assemblages that contain at least one mineral that exhibits diagnostic spectral absorption features. The broad phyllic zone is characterized by illite/muscovite (sericite), and quartz. Muscovite and illite exhibit an intense Al-OH spectral absorption feature typically cantered at 2.20 μm (ASTER band 6; Fig. 4a), and a less intense feature near 2.38 μm (ASTER band 8; Fig. 4a) [38]. In addition, phyllic zone rocks are commonly stained by jarosite, goethite, and hematite which exhibit a prominent spectral absorption feature near 0.44 μm in blue band of ETM$^+$ (ETM$^+$ Band 1; Fig. 5a).

The argillic zone can be indexed by kaolinite and montmorillonite, which shows an Al-OH absorption feature near 2.20 μm (ASTER band 6, Fig. 4a); they show markedly different spectral shapes to those of muscovite and illite [28,29]. Kaolinite shows a secondary feature or shoulder at 2.17 μm (ASTER band 5, Figs. 4a and 5a).

In the propylitic zone, reflectance spectra of the mineral assemblage are characterised by Fe, Mg-OH absorption features, and CO_3 features caused by molecular vibrations in epidote, chlorite, and carbonate minerals. These absorption features are situated in the 2.35 μm (ASTER band 8, Figs. 4a and 5a) region [47,

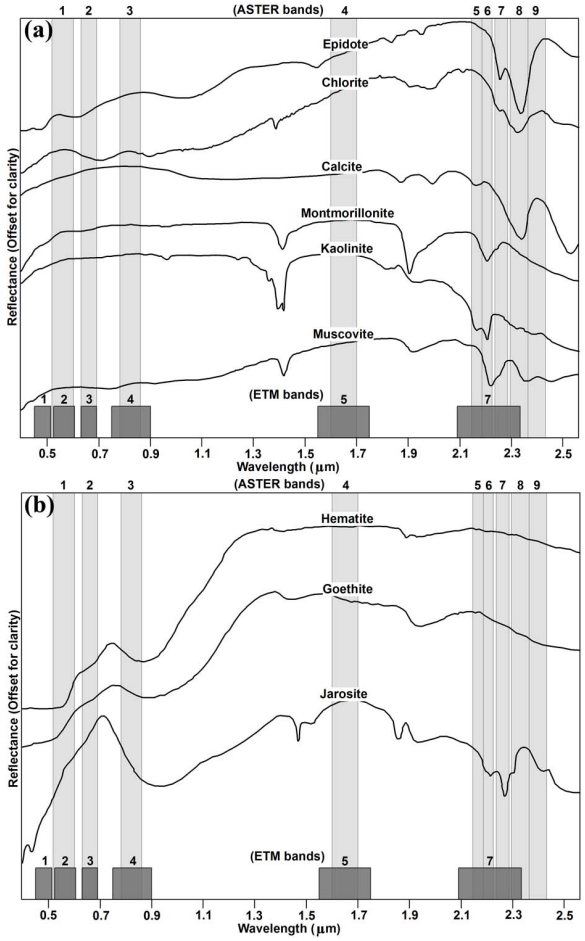

Figure 4. (a) Laboratory reflectance spectra of important hydrothermal alteration minerals and (b) iron oxide/hydroxide minerals (The spectra are taken from Livo et al. [35]).

38]. The clay, sericite, chlorite, epidote, and calcite minerals show high reflection in band 4 of ASTER data (Figs. 4a and 5a).

ETM^+ has more bands in the VNIR spectral regions than ASTER. Band 1 of ETM^+ is associated with ferric-iron absorption, and bands 2 and 3 are located in the reflective parts of the spectra for hematite, goethite, and jarosite (Figs. 4b and 5b).

Figure 5 (a-b) shows the spectra of field samples from various alteration zones, as measured by a spectroradiometer. The spectra of the samples from the phyllic zone show strong absorption features at 2.2 and 2.4 µm, whereas kaolinite in the argillic zone shows absorption features at 2.18 and 2.4 µm. The jarosite, goethite and hematite minerals, associated with the phyllic zone, show strong reflectance at 0.74 µm and absorption at 0.4 µm. The absorptions coinciding with band 6 of ASTER in the field spectra representing jarosite and goethite are due to the fact that, the samples are also sericite bearing, such that they are stained with jarosite and goethite coatings at the surface (Figs. 5a and 5b). The propylitic zone, which is characterised by chlorite, has strong absorption at 2.35 µm (Fig. 5a). Figure 6 shows the resulting image-derived spectra (endmembers) extracted from phyllic, argillic and propylitic alteration zones in the VNIR/SWIR data. A comparison between the spectra (for the ASTER and ETM bands regions) from image pixels, spectra from the USGS spectral library and measured in the field (Figs.4-6), indicate sufficient the similarity between the three spectral measurement types, such that they can be all used as a basis for deriving alteration maps using the ASTER and ETM imagery. In this case the field derived spectra were used as a basis for the image processing methods, as described in the next section.

Principal Components Analysis

PCA determines the eigenvectors of a variance–covariance or a correlation matrix. The resulting components are often more interpretable than are the original images. PCA is widely used for mapping the distribution of alteration in metallogenic provinces [e.g., 31,12,36,48,53,13,24,43,54,58]. PCA can be applied to multivariate datasets, such as multispectral remote sensing images, with the aim of highlighting spectral responses related to specific minerals produced by hydrothermal alteration [13]. In selective PCA analysis, only certain bands are chosen that contain absorption and reflection features of the mineral of interest. A reduction in the number of input channels results in an increased chance of defining a unique principal component for a specific mineral class [36,48].

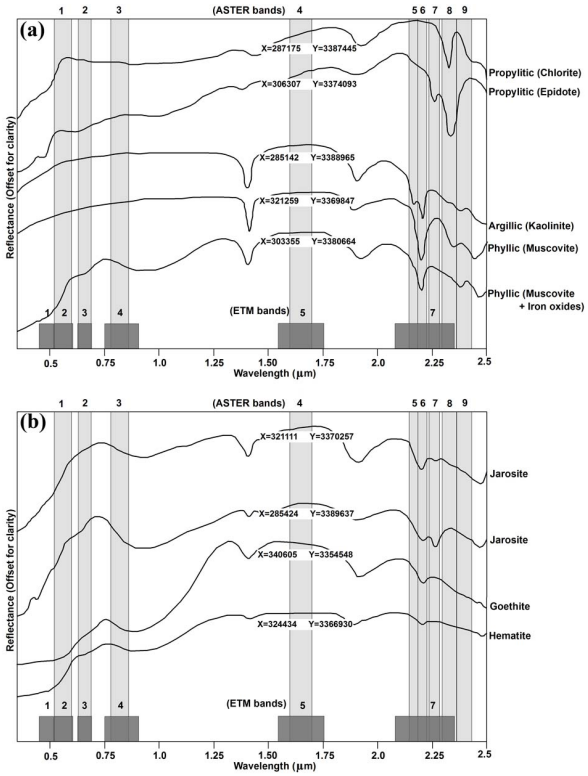

Figure 5. (a) The reflectance spectra of the hydrothermal minerals within the alteration zones and (b) iron oxide/hydroxide minerals, measured using a portable field radiometer. The geographical coordinates for each spectrum is shown in the figure.

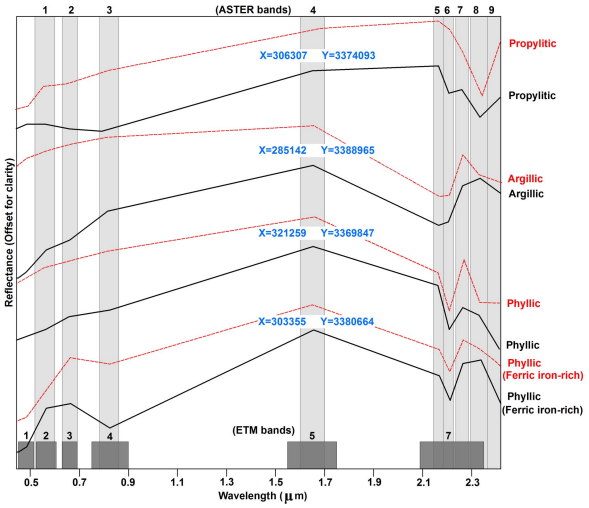

Figure 6. The reflectance spectra of altered rock samples from phyllic, argillic and propylitic alteration zones, measured by using portable field radiometer, resampled to the ASTER and ETM data (dotted line). Solid lines show the representative pixel spectral z-profiles extracted from ASTER and ETM images for the same location as rock samples' spectra. The geographical coordinates for the spectra are shown on the figure.

Endmember Extraction and Image Classification

It is a challenging task to identify endmember pixels whose spectra are extreme, especially in high–dimensional image data. This difficulty arises because most pixels contain varying proportions of different materials [33, 46, 4]. A spectral mixture model is a physically based model in which a mixed spectrum is modelled as a combination of pure spectra that are referred to as endmembers. The extraction of endmembers is commonly based on rigorous mathematical algorithms.

The minimum noise fraction (MNF) transformation was used to reduce the data redundancy and extract features for classification. Noise can be effectively removed from multispectral data by transformation to the MNF space, smoothing or rejecting the most noisy components, and then retransformation to the original space [18, 9, 17, 15, 58]. The MNF transform applied to the ASTER data achieved a reasonable separation of coherent signal from complementary noise; consequently, the MNF transformed eigen–images were employed and coupled with PPI and n–dimensional visualization techniques to facilitate extraction of the major endmembers in the scene.

The PPI is a means of finding the most spectrally pure or extreme pixels in multispectral and hyperspectral images from higher–order MNF eigen–images, using the convex geometry argument [10]. This algorithm selects pixels whose spectra are extreme or spectrally pure and therefore represent the most suitable spectral categories. N–dimensional (n–D) visualization techniques enable the simultaneous analysis of all the spectral information embedded in a full scene [7]. Following the application of the PPI algorithm, the n–D visualizer is used to locate, identify, and cluster the purest pixels and the most extreme spectral responses in a data set.

PPI was applied over the first six MNF images that were extracted from ASTER VNIR/SWIR bands with higher eigenvalues that contain 93.83% of the total data variance. The remaining MNF components contain noise [18]. The spectra of individual endmembers were then derived from the original images, based on their spatial location. To enable the identification of minerals, these spectra were compared with known spectra from the USGS spectral library and with data from samples collected in the field as part of ground truthing (i.e. XRD analysis, observations of thin sections, and spectral measurements).

In this study, SAM and LSU were used for mapping the distribution of alteration zones. The SAM is a supervised image classification method that allows rapid mapping of the degree of similarity between image spectra and reference spectra. The reference spectra can be chosen from either laboratory or field spectra, or extracted from the image. This method assumes that the data have been reduced to apparent reflectance, with all dark current and path radiance biases removed. SAM compares the angle between the reference spectrum and each pixel vector in n-dimensional space, with smaller angles indicating a closer match to the reference [33]. The SAM algorithm has previously been applied to hyperspectral and multispectral data for mapping the distribution of hydrothermal alteration [e.g., 26, 27, 17, 44, 55, 54, 21].

LSU method determines relative abundances of materials being depicted in multi or hyper-spectral imagery based on their spectral characteristics [8]. An important assumption of LSU is that the reflectance at each pixel of the image is the linear proportion-weighted combination of the reflectance of each endmember present within the pixel. The number of endmembers must be no more than n+1, where n is the number of spectral bands [16]. The results of spectral unmixing appear as a series of gray-scale images, one for each endmember with values from 0.0 to 1.0, plus a root-mean-square (RMS) error image. Higher abundances (and higher errors for the RMS error image) are represented by brighter pixels. Spectral unmixing results are highly dependent on the input endmembers, and changing the endmembers changes the results.

The accuracy of the classified images can be quantified. The most commonly employed method of expressing classification accuracy is the preparation of a classification error matrix or confusion matrix [11]. This approach was used to assess the accuracy of the images using the SAM and LSU approaches.

Table 3. Eigenvector loadings for 3 bands of ASTER data

	PC1	PC2	PC3	Alteration minerals
Band 4	0.62	-0.46	-0.63	muscovite/sericite (phyllic zone)
Band 6	0.53	-0.33	0.78	
Band 7	0.57	0.04	-0.82	
% of variance	98.55	0.64	0.81	
Band 4	0.63	0.76	0.10	kaolinite/ montmorillonite (argillic zone)
Band 5	0.55	-0.37	0.75	
Band 6	0.54	-0.52	-0.66	
% of variance	98.34	0.67	0.99	
Band 7	0.61	-0.78	-0.14	chlorite/epidote (propylitic zone)
Band 8	0.56	0.54	0.63	
Band 9	0.56	0.31	-0.76	
% of variance	99.11	0.48	0.41	

Results and Discusion

To map the distribution of alteration, we applied a selective PCA technique. To determine which image contains information related to the spectral signatures of specific target minerals, we employed an approach based on an examination of eigenvector loadings in each PC image. The PC image with moderate to high eigenvector loadings for the diagnostic absorptive and reflective bands of the index mineral is considered the specific image for that mineral. If the loading of the absorptive band is negative in sign, the target area is shown by bright pixels; if the loading of the reflective band is negative, the area is shown by dark pixels [12].

The main alteration types in the study area are phyllic, argillic, and propylitic. Table 3 lists the results of PCA on three ASTER bands. The bands were chosen based on the spectral characteristics of the alteration minerals. According to the eigenvector loadings of each of the three bands (Table 3), in PC3 (all three data sets), areas with minerals characteristic of the phyllic, argillic, and propylitic zones are shown as dark pixels. To show the areas containing hydrothermal alteration minerals as bright pixels, we obtained the inverse of PC3. PC3 image shows areas containing muscovite, kaolinite/ montmorillonite, and chlorite/epidite in three alteration zones associated with porphyry copper deposits. Figure 7 shows an image produced by the addition of PC3 (phyllic) and PC3 (argillic). This image reveals the distribution of alteration haloes related to hydroxyl-bearing minerals in and around areas of porphyry copper mineralization. Areas of phyllic and argillic alteration are indicated by bright pixels in porphyry copper deposits such as those at Kader, Godekolvary, Iju, Serenu, Chahfiroozeh, Parkam, Meiduk, and Abdar. The third PC (propylitic; Table 3) highlights areas of propylitic alteration because it contains higher loadings for bands 8 and 9, which have opposite signs to each other. The inverse of this PC is shown in Figure 8. The central phyllic/argillic zones (dark pixels) are surrounded by bright pixels related to the propylitic zone. Some northeastern and eastern areas in the image are also enhanced as bright pixels, corresponding to flysch and coloured mélange units, due to the spectral similarities between the minerals of the propylitic zone and those of the flysch and coloured mélange.

Selected PCA was also applied to subsets of two ASTER bands and two VNIR bands of ETM^+, using a modified version of the Crosta technique (Table 4). The selection of four bands as input for PCA was based on laboratory analyses and image spectra of the minerals associated with hydrothermal alteration and iron oxide/hydroxide minerals in the VNIR and SWIR regions (Figs. 4–6).

The PCA eigenvector statistics for these bands (PC4) show high loadings with opposite signs for bands 6 (0.47) and 7 (–0.52) for muscovite/sericite (phyllic zone), and for bands 4 (–0.70) and 5 (0.70) for kaolinite/montmorillonite (argillic zone). Because these two alteration zones are associated with iron oxide/hydroxide minerals, bands 1 and 3 of ETM^+ also have high loadings with opposite signs in PC4. Consequently, areas of phyllic and argillic alteration associated with goethite, jarosite, and hematite are shown as dark pixels; although field investigations reveal that iron oxide minerals are more abundant in phyllic zone than in argillic zone. PC4 enhances the zone of propylitic alteration because of high loadings of bands 8 and 9 for chlorite/epidote (propylitic zone). Lower loadings of bands 1(–0.06) and 3 (0.05) in PC4 are indicating that iron oxide/hydroxide minerals are not associated with the propylitic zone.

Figure 9 shows the inverse of PC4 (argillic zone; red), inverse of PC4 (phyllic zone; green), and inverse of PC4 (propylitic zone; blue) in RGB. White areas indicate zones of phyllic and argillic alteration associated with iron oxide/hydroxide minerals. The propylitic zone is shown as a greenish colour.

As this study aimed to map the distribution of haloes of hydrothermal alteration around areas of porphyry copper mineralization, the spectra of selected alteration minerals, as obtained from field samples, were used as reference spectra for SAM. These minerals were selected based on the results of field studies, XRD analyses, and spectral measurements. Muscovite (sericite) and illite are representatives of the phyllic zone; kaolinite and montmorillonite are representative of the argillic zone, and chlorite and epidote are representatives of the propylitic zone. Jarosite, goethite, and hematite were also selected as secondary minerals in the phyllic zone. Figures 10 and 11 show the results obtained using the SAM method. The SAM method was used to map the distribution of phyllosilicate/chlorite/epidote minerals in their respective alteration zones and also in the ferric-iron-rich phyllic zone (Fig. 10). As shown in Figure 5a, the phyllic zone shows two spectra. These two spectra were used to generate ferric-iron-rich phyllic zones and phyllic zones (Fig. 10). To create the alteration map shown in Figure 10, a threshold value of 0.06 radians was used for the phyllic and argillic zones, 0.05 radians was used for the propylitic zone, and 0.05 radians for goethite, jarosite, and hematite. These threshold values were selected in conjunction with field-based ground–truthing and the results of previous remote sensing-based mapping studies [e.g., 38]. Each alteration zone

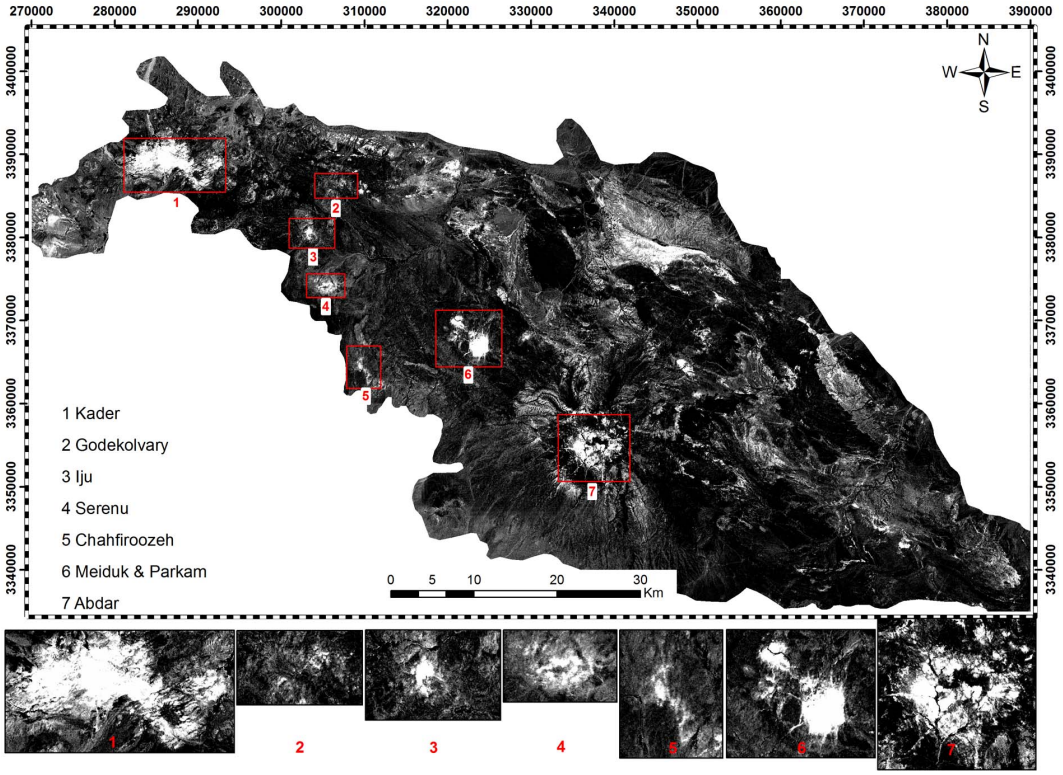

Figure 7. The inverse of PC3 (phyllic, Table 3) + PC3 (argillic, Table 3) that highlights the hydroxyl minerals bearing areas.

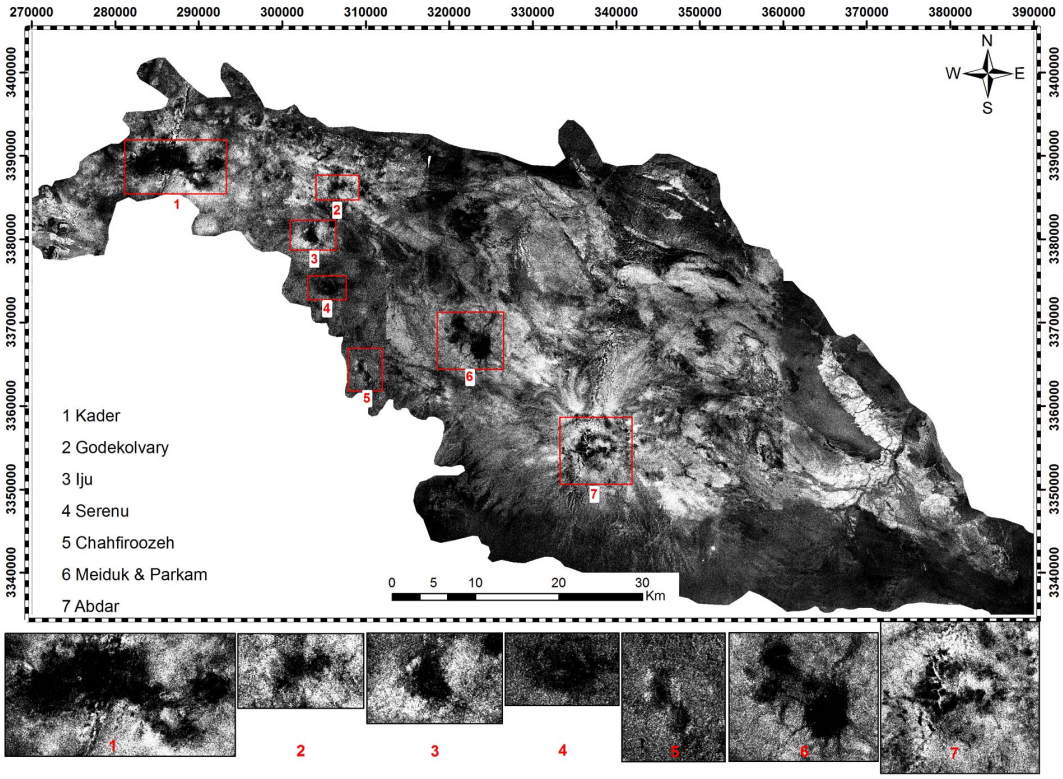

Figure 8. The image shows inverse of PC3 (Table 3) that depicts the areas affected by propylitic alteration (bright pixels).

Table 4. Eigenvector loadings for 4 bands of ASTER and ETM data

	PC1	PC2	PC3	PC4	Alteration minerals
Band 1 (ETM)	0.50	0.55	0.41	0.53	muscovite +iron oxide/hydroxide minerals (phyllic zone)
Band 3 (ETM)	0.50	0.44	-0.57	-0.48	
Bnad 6 (ASTER)	0.50	-0.60	-0.41	0.47	
Band 7 (ASTER)	0.50	-0.38	0.57	-0.52	
% of variance	76.32	19.18	2.74	1.76	
Band 1 (ETM)	0.49	0.56	0.56	0.15	kaolinite/montmorillonite +iron oxide/hydroxide minerals (argillic zone)
Band 3 (ETM)	0.50	0.44	-0.47	-0.20	
Band 4 (ASTER)	0.50	-0.51	-0.05	-0.70	
Band 5 (ASTER)	0.50	-0.48	0.14	0.70	
% of variance	74.22	22.63	1.98	1.17	
Bnad 1 (ETM)	0.49	-0.54	-0.67	-0.06	chlorite/epidote (propylitic zone)
Band 3 (ETM)	0.50	-0.46	0.73	0.05	
Band 8 (ASTER)	0.50	0.51	0.02	-0.70	
Band 9 (ASTER)	0.50	0.49	-0.08	0.71	
% of variance	76.68	20.98	1.52	0.82	

was mapped separately and showed on a base image of ASTER band 1 (Figs. 10 and 11).

Five main endmembers were identified, using the PPI technique, from the six MNF images: muscovite/ illite (phyllic), kaolinite/monmorillonite (argillic), chlorite/ epidote (propylitic), unaltered units in volcanic rocks, and green vegetation. There are some overlaps in the occurrence of associated minerals. Since the aim of this research was to map the alteration minerals and to estimate their abundances near copper–mineralization districts at the study area rather than mapping all the exposed lithological units, the output results of diagnostic alteration endmembers including phyllic, argillic, and propylitic were discussed. In this study, we sought to map the distribution of three alteration zones over the eight copper–mineralization districts by using the endmembers derived from the n–dimensional endmember visualization method as reference spectra for LSU classification. Figure 12 shows the final image that resulted from LSU analysis. In this Figure each alteration zone was assigned a unique colour and was displayed over a gray scale image. Phyllic zone is depicted in dark red and red colours which highlight the intense phyllic and phyllic alteration respectively. Comparison of Figures 10 and 12 shows that the areas which are shown as intense phyllic zone in Figure 12 is overlapping the areas with ferric iron-rich phyllic zone in Figure 10.

The field and laboratory results show that SAM and LSU enable the identification of different alteration zones around porphyry copper deposits in the study area (Table 5). In the Kader area, three zones of hydrothermal alteration are relatively uniform over an area that includes zones of phyllic, argillic, and propylitic alteration. Figure 13a shows a photograph of an outcrop of the argillic zone in the Kader area. The feldspars in the altered rocks are converted to kaolinite, illite, and sericite (Fig. 13b). Because of the difficulties in identification of clay minerals in thin section, we analyzed the rock samples by XRD and spectroradiometer (Figs. 13c and 13d). Argillic alteration is present in the deposits at Kader, Serenu, Meiduk, Parkam, Godekolvary and Abdar (Table 5). Sericite alteration is dominant at the Iju, Serenu, Chahfiroozeh, Meiduk, Parkam, Kader, and Abdar porphyry copper deposits. Two types of phyllic alteration can be identified, both in the field and from processed satellite images, enabling the discrimination of outcrops of phyllic alteration (Fig. 14) and ferric-iron-rich phyllic alteration (intense phyllic) (Fig. 15). Although a small amount of iron oxide minerals is present in the phyllic alteration, absorption of the blue band was not apparent in the rock spectra (Fig. 14d). The iron-oxide-rich phyllic zone contains a large amount of iron oxide minerals on the surface, and shows strong absorption in the blue band (Fig. 15c). The iron oxide/hydroxide minerals are in the form of goethite, jarosite and minor hematite (see Fig. 5b), which are common secondary minerals at the Kader, Iju, Serenu, Parkam, Meiduk, and Abdar deposits.

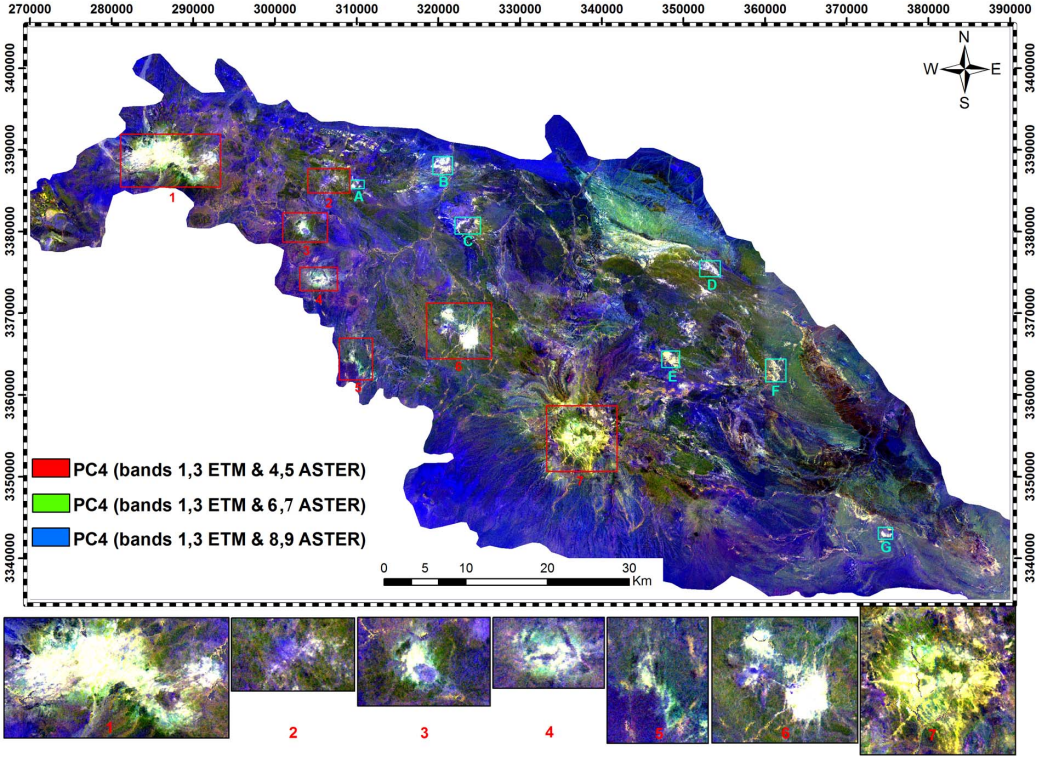

Figure 9. The colour combinations of PC4 (argillic zone in red), PC4 (phyllic zone in green) and PC4 (propylitic zone in blue). Bright Pixels show phyllic and argillic alteration zones associated with iron oxide/hydroxide minerals. Propylitic zone is shown in greenish colour.

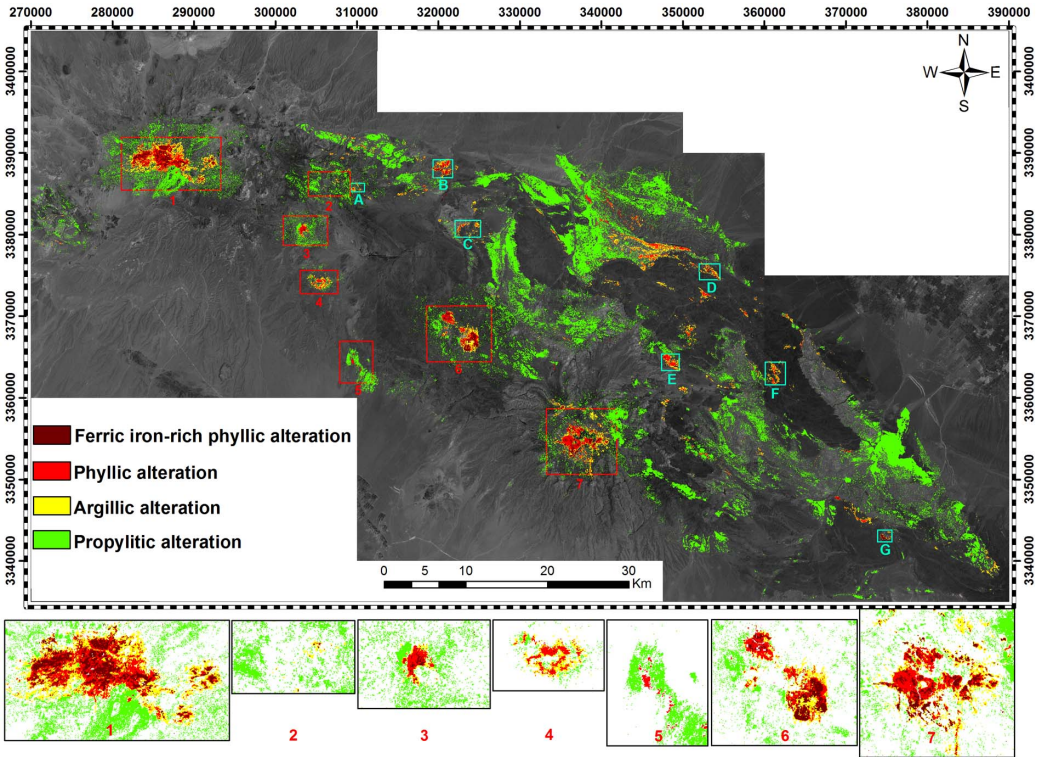

Figure 10. The result of SAM classification for alteration minerals, overlain on ASTER band 1 image.

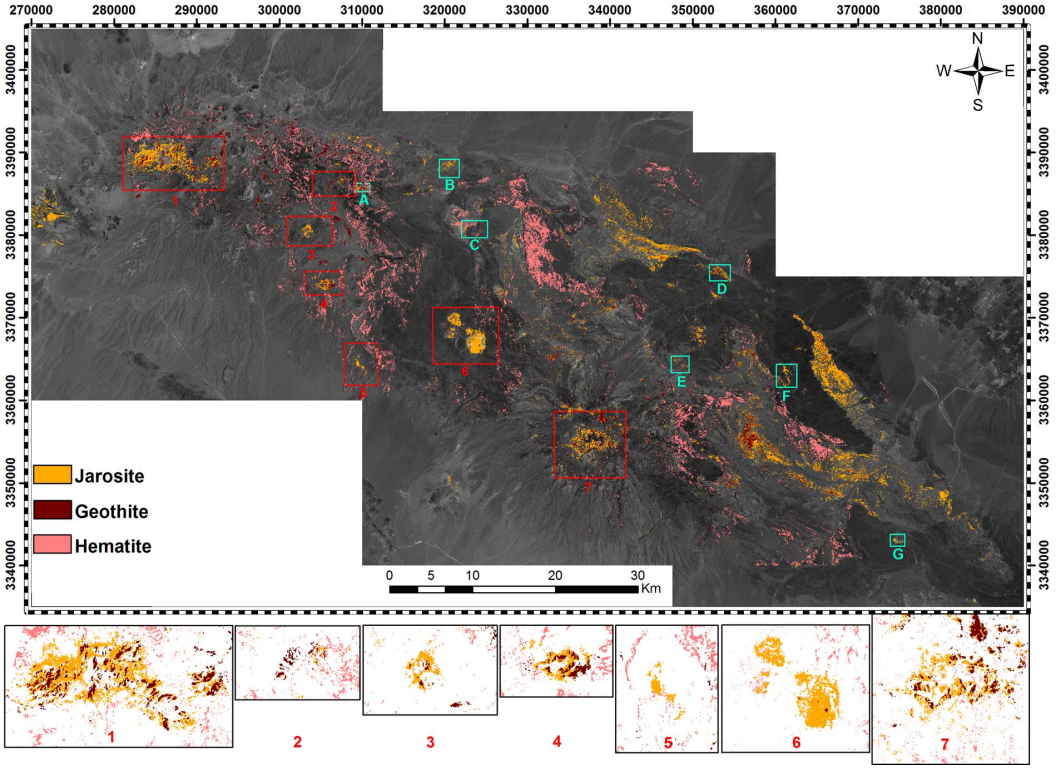

Figure 11. The result of SAM classification for iron oxide/hydroxide minerals, overlain on ASTER band 1 image.

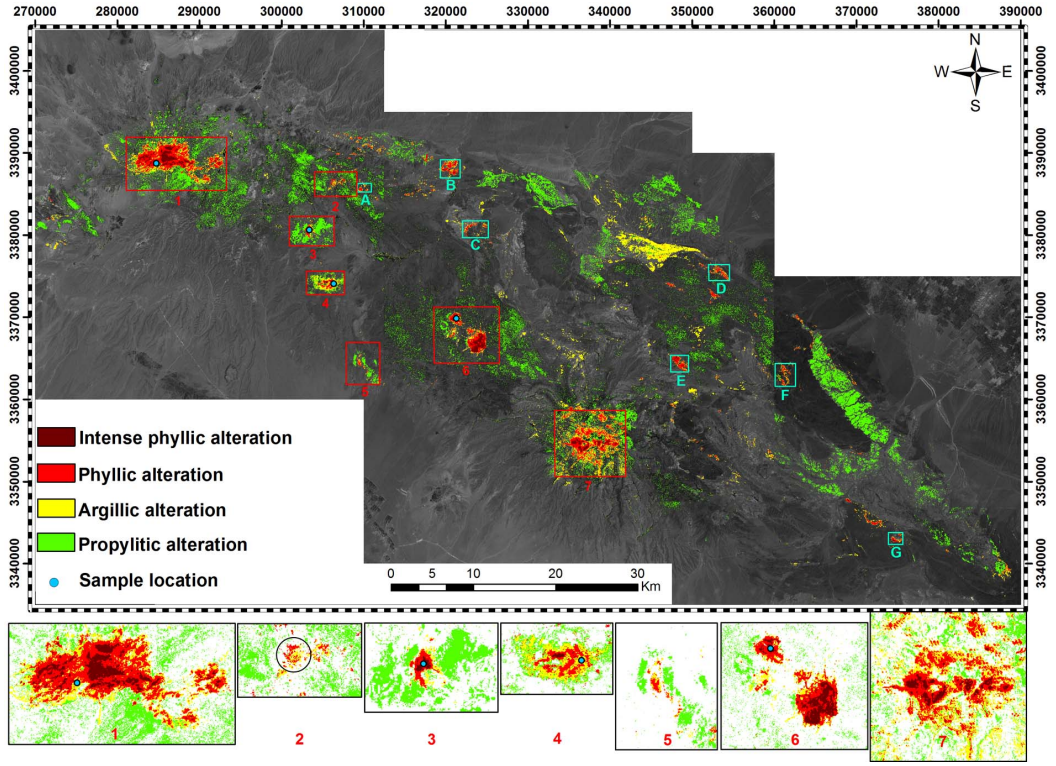

Figure 12. LSU processing results for hydrothermal alteration mapping by using the endmember spectra, around porphyry type deposits in the study area, overlain on ASTER band 1 image. Sample location of Fgures 13-16 are shown by blue dots.

Table 5. Alteration types and geochemical characteristics of the major copper deposits in the study area

	Deposit	Main alteration types*	Main Altered minerals*	Cu†(ppm)	Mo†(ppm)
1	Kader	Phyllic, Argillic, Propylitic, Silicification	Muscovite, Kaolinite, Illite, Quartz, Natroalunite	94 (8)	6.5 (8)
2	Godekolvary	Argillic, Phyllic, Propylitic, Silicification	Kaolinite, Muscovite, Montmorillonite, Quartz, Chlorite, Epidote	180 (4)	17 (4)
3	Iju	Phyllic, Argillic, Potassic, Propylitic, Jarositization	Muscovite, Illite, Quartz, Kaolinite, Albite, Chlorite	220 (20)	20 (20)
4	Serenu	Phyllic, Argillic, Propylitic, Potassic	Muscovite, Illite, Quartz, Albite, Orthoclase, Kaolinite, Chlorite Montmorillonite	108 (11)	6.9 (11)
5	Chahfiroozeh	Phyllic, Potassic, Propylitic	Muscovite, Illite, Quartz, Albite, Orthoclase	438 (14)	8.5 (14)
6	Parkam	Phyllic, Argillic, Potassic, Propylitic, Jarositization, Silicification	Muscovite, Illite, Quartz, Jarosite, Albite, Orthoclase, Kaolinite	210 (5)	5.4 (5)
7	Meiduk	Phyllic, Argillic, Potassic, Propylitic	Muscovite, Illite, Quartz, Jarosite, Albite, Orthoclase, Kaolinite, Montmorillonite	N.A	N.A
8	Abdar	Phyllic, Argillic, Propylitic	Muscovite, Illite, Quartz, Albite, Kaolinite, Montmorillonite, Chlorite	145 (9)	7 (9)
9	Palangi	Carbonatization, Propylitic, Chloritization, Sericitization, Silicification	Chlorite, Epidote, Calcite, Quartz	N.A	N.A
10	Chahmesi	Propylitic, Silicification	Chlorite, Epidote, Quartz	N.A	N.A

*based on field observations, thin section studies, spectral measurements and XRD analysis.
† Mean values. Number of samples are shown in brackets. Chemical analysis by inductively coupled plasma (ICP). The samples are taken randomly from the outcrops in the phyllic and argillic zones. N. A= Not available.

Table 6. Accuracy assessment matrices for SAM and LSU methods

	Phyllic	Argillic	Propylitic	Unaltered	Total	Percent
a) Classification accuracy assessment for the spectral angle mapper (SAM) approach						
Phyllic	89	2	5	2	98	90.82
Argillic	13	24	6	2	45	53.33
Propylitic	5	2	44	1	52	84.61
Unaltered	7	6	8	11	32	34.37
Total	114	34	63	16	227	
Percent	78.07	70.59	69.84	68.75		74.01
Kappa coefficient: 0.65						
b) Classification accuracy assessment for the linear spectral unmixing (LSU) approach						
Phyllic	95	2	2	1	101	94.06
Argillic	8	27	3	1	39	69.23
Propylitic	5	0	50	1	55	90.91
Unaltered	6	5	8	13	32	40.62
Total	114	34	63	16	227	
Percent	83.33	79.41	79.36	81.25		81.50
Kappa coefficient: 0.71						

Because of the presence of minerals such as chlorite and epidote, the spectra of propylitic rocks show strong absorption in 2.33 μm (Fig. 16). Propylitic alteration occurs around most of the mineralized areas. In addition, vein-type mineralization in the area is affected by propylitic alteration. As an example, the Palangi copper deposit is a deposit most strongly dominated by propylitic alteration.

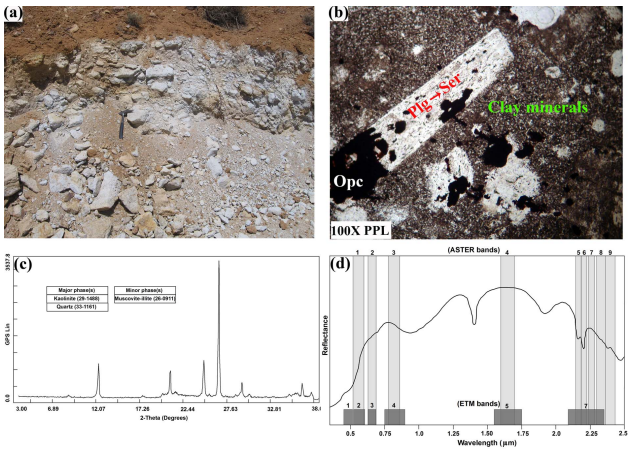

Figure 13. (a) An outcrop of argillic alteration in Kader area, (b) thin section of a rock sample collected from (a) that shows the conversion of feldspars into kaolinite, illite and sericite, (c) XRD of a rock sample which shows the peaks related to the minerals such as kaolinite, quartz, muscovite and illite, and (d) spectra of a sample collected from outcrop shown in (a). Sample location is shown in Figure 12. Plg: plagioclase; Ser: sericite; Opc: opaque minerals.

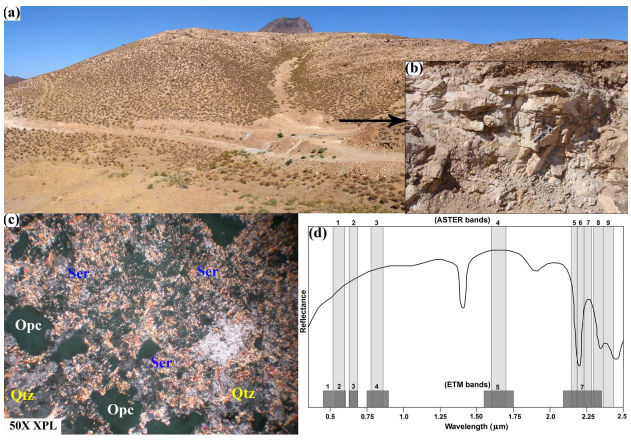

Figure 14. (a) General view of phyllic alteration in Parkam deposit, (b) outcrop of phyllic alteration, (c) thin section of the altered rock that shows abundant sericite, quartz and opaque minerals, and (d) Spectra of a rock sample from phyllic zone collected from (b). Sample location is shown in Figure 12. Ser-sericite; Qtz-quartz; Opc-opaque minerals.

Areas A through G (mapped in Figs. 9-12) contain zones of argillic and phyllic alteration. Field investigations revealed that these areas are not associated with mineralization.

To assess the accuracy of the image processing results, 15 field sites were selected for ground control and sampling, from where 227 samples were collected. This follow-up work included visits to all the known sites of copper mineralization reported in the previous studies, as well as alteration zones identified in the present study (Table 5), in an attempt to better understand the nature of hydrothermal alteration in each site. At each station, we performed field observations, took global positioning system (GPS) readings, collected samples for petrographical/XRD analysis, and took field photographs. The spectra of the representative samples from altered zones were also measured using a spectroradiometer. Areas A–G (Figs. 9–12) were also sampled and the enhanced altered areas include kaolinitization and sericitization accompanied by silicification. Field observation showed that these areas have weaker alteration compared with the mineralized areas.

Table 6 shows the accuracy assessment matrix of the SAM and LSU analysis results based on 227 samples. Although visual comparison of the SAM and LSU images for hydrothermal alteration mapping (Figs. 10 and 12), in general, show similar results, detailed direct comparison of the mapping results using a confusion matrix approach demonstrates that their similarities are not as great as may be thought from visual comparison. A detailed direct comparison of the mapping results using a confusion matrix approach reveals that the LSU method has a higher accuracy (81.5%; kappa coefficient, 0.71) than SAM classification method (74.01%; kappa coefficient, 0.65).The LSU method is superior to the SAM classification method in its ability to enhance various alteration zones, especially in the Kader, Godekolvary, Serenu, and Abdar areas (compare Figs 10 and 12). There exists one alteration zone in the Godekolvary area which is enhanced in the LSU image (as outlined in Figure 12 by black circle, but is not prominent in the SAM classification image). The argillic zone in the Kader area is more strongly enhanced in the LSU image than in the SAM image. The extent of the enhanced argillic zone in the SAM image is inaccurate. Compared with the SAM image, the propylitic zone is more accurately enhanced in all areas in the LSU image.

SAM depends on an overall spectral fit rather than the shape of individual, diagnostic absorption features [21]. In contrast, the LSU is a mixed pixel classification in which a partial unmixing method suppresses

background noise and estimates the sub–pixel abundance of a single target material. This may explain why the LSU technique yielded a better result than did the SAM method. The results obtained for various sites of mineralization indicate that the LSU mapping method can be used to produce a reliable alteration map at the preliminary stage of mineral exploration and this algorithms can be used for further exploratory investigations.

Three–band directed principal component analysis was successful in highlighting the distribution of individual alteration minerals (sericite, kaolinite, illite, chlorite, and epidote) present in the alteration zones of the northwestern part of the Kerman Cenozoic magmatic arc, southeast Iran. Although ASTER data do not contain the blue band, a combination of ETM^+ and ASTER data can be used in mapping the distribution of iron oxide/hydroxide minerals. The application of directed principal component analysis (DPCA) to combined ETM^+ and ASTER data reveals the distribution of areas of phyllic/argillic alteration that are associated with iron oxide/hydroxide minerals. The supervised classification of ASTER and ETM^+ data using spectral angle mapper (SAM) results in more accurate maps of alteration than those obtained using DPCA. The spectra derived from the PPI method were used as reference spectra in the linear spectral unmixing (LSU) method, which produced a more accurate classification than that obtained using the SAM method. Field studies confirmed that the LSU method is reliable in terms of mapping alteration haloes during the preliminary stages of exploration for porphyry–type mineralization. Samples of altered rocks were subjected to XRD analysis and observed in thin section under the microscope. Field studies revealed that less than 10% of the mineralized areas (mainly vein-type mineralization) are unrelated to zones of phyllic/argillic alteration.

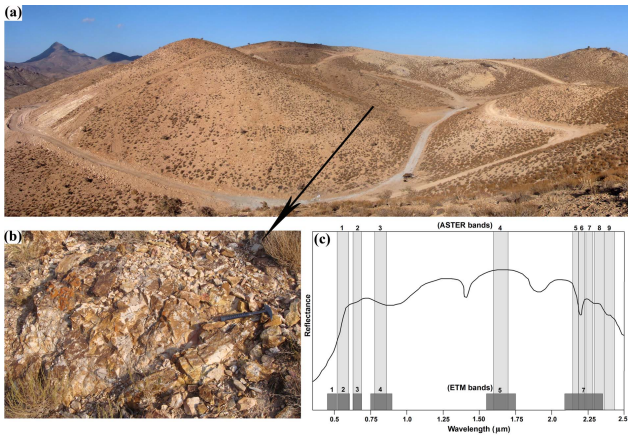

Figure 15. (a) General view of the ferric iron-rich phyllic zone in Iju area, (b) outcrop of a phyllic zone that has goethite and jarosite minerals at the surface, and (c) spectra of a sample collected from phyllic zone (b) that shows blue band iron oxide absorption.Sample location is shown in Figure 12.

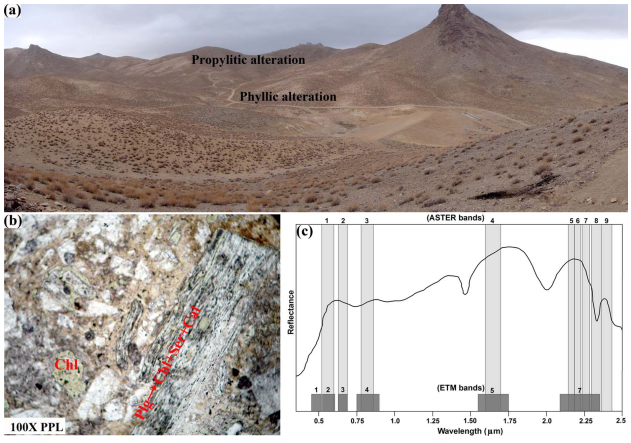

Figure 16. (a) General view of phyllic and propylitic alterations in Serenu area, (b) thin section of a rock sample that is rich in chlorite, and (c) spectra of a rock sample with propylitic alteration shown in (b). Sample location is shown in Figure 12. Chl-chlorite; Plg-plagioclase; Ser-sericite.

Acknowledgments

The Kerman Office of Mines and Industries and national Iranian copper industries company (NICICo) are thanked for providing the logistics for field visits and sample collections. We thank the Technical University of Kerman in Mahan for providing FieldSpec3® spectroradiometer. The authors acknowledge constructive reviews from anonymous reviewers of the Journal of Sciences, Islamic Republic of Iran which helped to improve the manuscript.

References

1. Abrams J., Brown D., Lepley L., and Sadowaski R. Remote sensing for porphyry copper deposits in Southern Arizona. *Econ. Geol.,* **78**(4): 591-604 (1983).
2. Alavi M. Tectono-stratigraphic evolution of the Zagrosside of Iran. *Geology*, **8**(3): 144–149 (1980).
3. Bazin D., and Hubner H. *Copper deposits in Iran*. Geological Survey of Iran publication, Tehran, Rep.,13, 232 p. (1969).
4. Bedini E., Van Der Meer F., and Van Ruitenbeek F. Use of HyMap imaging spectrometer data to map mineralogy in the Rodalquilar caldera, southeast Spain. *Int. J. Remote Sens.,* **30**: 327–348 (2009).
5. Ben-Dor E., and Kruse F. A. The relationship between the size of spatial subsets of GER 63 channel scanner data and

the quality of the Internal Average Relative Reflectance (IARR) atmospheric correction technique. *Int. J. Remote Sens.*, **15**(3): 683-690 (1994).

6. Boomeri M., Nakashima K., and Lentz D.R. The Miduk porphyry Cu deposit, Kerman, Iran: A geochemical analysis of the potassic zone including halogen element systematics related to Cu mineralization processes. *J. Geochem. Exploration*, **103**(1): 17-29 (2009).
7. Boardman J.W. Automated spectral unmixing of AVIRIS data using convex geometry concepts. In *Summaries, Fourth JPL Airborne Geoscience Workshop*, JPL Publication 93–26, **1** (Pasadena, CA: Jet Propulsion Laboratory): 11–14 (1993).
8. Boardman J.W. Leveraging the high dimensionality of AVIRIS data for improved sub–pixel target unmixing and rejection of false positives: mixture tuned matched filtering. In *Summaries of the 7th Annual JPL Airborne Geoscience Workshop*, Pasadena, CA (Pasadena, CA: Jet Propulsion Laboratory), 55–56 (1998).
9. Boardman J.W., and Kruse F.A. Automatic spectral analysis: a geological example using AVIRIS data, North Grapevine Mountain, Nevada. In *10th Thematic Conference on Geologic Remote Sensing*, Ann Abor (Environmental Research Institute of Michigan), 407–418 (1994).
10. Boardman J.W., Kruse F.A., and Green R.O. Mapping target signatures via partial unmixing of AVIRIS data. In *Summaries, Fifth JPL Airborne Earth Science Workshop*, JPL Publication 95–1, **1** (Pasadena, CA: Jet Propulsion Laboratory), 23–26 (1995).
11. Congalton R. G. A review of assessing the accuracy of classifications of remotely sensed data. *Remote Sens. Environ*, **37**: 35–46 (1991).
12. Crosta A.P., and Moore J.M. Enhancement of Landsat Thematic Mapper imagery for residual soil mapping in SW Minais Gerais State, Brazil: a prospecting case history in Greenstone Belt Terrain. In Proceedings of the Seventh Thematic Conference on Remote Sensing for Exploration Geology, 2-6 October, Calgary, Canada, *ERIM*, 1173–1187 (1989).
13. Crosta A.P., DE Souza Filho C.R., Azevedo F., and Brodie C. Targeting key alteration minerals in epithermal deposit in Patagonia, Argentina, using ASTER imagery and principal component analysis. *Int. J. Remote Sens.*, **10**(21): 4233-4240 (2003).
14. Dimitrijevic M.D. *Geology of the Kerman region*. Geological Survey of Iran publication, Tehran, Rep., 52, 334 p.(1973).
15. Ducart D.F., Crosta A. P., Souza Filho C. R. and Coniglio J. Alteration mineralogy at the Cerro La Mina epithermal prospect, Patagonia, Argentina: Field mapping, short-wave infrared spectroscopy, and ASTER images. *Econ. Geol.*, **101**: 981-996 (2006).
16. Ferrier G., White K., Griffiths G., Bryant R., and Stefouli M. The mapping of hydrothermal alteration zones on the island of Lesvos, Greece using an integrated remote sensing dataset. *Int. J. Remote Sens.*, **23**(2): 341–356 (2002).
17. Galvao L.S., Almeida-Filho R., and Vitorello Í. Spectral discrimination of hydrothermally altered materials using ASTER short-wave infrared bands: Evaluation in a tropical savannah environment. *Int. J. Appl. Earth Observation Geoinformation*, **7**(2): 107-114 (2005).
18. Green A.A., Berman M., Switzer P., and Craig M.D. A transformation for ordering multispectral data in terms of image quality with implications for noise removal. *IEEE Trans. Geosci. Remote Sens.*, **26**: 65–74 (1988).
19. GSI, 1973. *Exploration for ore deposits in Kerman region*. Geological Survey of Iran publication, Tehran, Rep., 53, 247 p.(1973).
20. Hassanzadeh J. Metallogenic and tectono-magmatic events in the SE sector of the Cenozoic active continental margin of Iran (Shahr-e-Babak area, Kerman province). Unpublished Ph.D. *Thesis*, University of California, Los Angeles, 204 p. (1993)
21. Hecker C., van der Meijde M., van der Werff H., and van der Meer F. D. Assessing the Influence of Reference Spectra on Synthetic SAM Classification Results. *IEEE Trans. Geosci. Remote Sens.*, **46**(12): 4162-4172 (2008).
22. Hezarkhani A. Hydrothermal evolution of the Sar-Cheshmeh porphyry Cu–Mo deposit, Iran: evidence from fluid inclusions. *J. Asian. Earth Sci.,* **28**(4-6): 409–422 (2006).
23. Hezarkhani A., Williams-Jones A.E., and Gammons C.H. Factors controlling copper solubility and chalcopyrite deposition in the Sungun porphyry copper deposit, Iran. *Mineral. Deposita*, **34**(8): 770–783 (1999).
24. Honarmand M., Ranjbar H., and Moezifar Z. Integration and analysis of airborne geophysics, remote sensing and geochemical data of Sar Cheshmah area, using directed principal component analysis. *Explor. Mining Geol.*, **11**(1-4): 43-48 (2004).
25. Hosseinjani M., and Tangestani M.H. Mapping alteration minerals using sub-pixel unmixing of ASTER data in the Sarduiyeh area, SE Kerman, Iran. Int. J. Digital Earth, **1**: 1–18 (2011).
26. Hubbard B.E., Crowley J.K., and Zimbelman D.R. Comparative alteration mineral mapping using visible to shortwave infrared (0.4–2.4 μm) Hyperion, ALI, and ASTER imagery. *IEEE Trans. Geosci. Remote Sens.*, **41**(6) :1401–1410 (2003).
27. Hubbard B.E., and Crowley J.K. Mineral mapping on the Chilean-Bolivian Altiplano using co-orbital ALI, ASTER and Hyperion imagery: data dimensionality issues and solutions. *Remote Sens. Environ.*, **99**(1): 173-186 (2005).
28. Hunt G.R. Spectral signatures of particulate minerals in the visible and near infrared. *Geophysics*, **42**(3): 501–513 (1977).
29. Hunt G.R., and Ashley R.P. Spectra of altered rocks in the visible and near infrared: *Econ. Geol.*, **74**(7): 1613–1629 (1979).
30. Iwasaki A., and Tonooka H. Validation of Crosstalk correction algorithm for ASTER/SWIR. *IEEE Trans. Geosci. Remote Sens.*, **43**(12): 2747-2751 (2005).
31. Kaufmann H. Mineral exploration along the Aquaba-levant structure by use of TM data, concepts, processing and Results. *Int. J. Remote Sens.*, **9**(10): 1639–1658 (1988).
32. Kruse F.A., Raines G.L., and Watson K. Analytical techniques for extracting geologic information from multichannel airborne spectroradiometer and airborne imaging spectrometer data. In International Symposium on

Remote Sensing of Environment, 4th Thematic Conference on Remote Sensing for Exploration Geology, 1-4 April, Ann Arbor, Michigan, *ERIM*, 309–324 (1985).
33. Kruse F.A., Lefkoff A.B., Boardman J.B., Heidebreicht H.K.B., Shapiro A.T., Barloon P.J., and Goetz A.F.H. The Spectral Image Processing System (SIPS)–interactive visualization and analysis of imaging spectrometer data. *Remote Sens. Environ.*, **44**(2-3): 145–163 (1993).
34. Kruse F. A., Boardman J., and Huntington J. F. Comparison of airborne hyperspectral data and EO-1 Hyperion for mineral mapping. *IEEE Trans. Geosci. Remote Sens.*, **41**: 1388–1400 (2003).
35. Livo K.E., Clarck R.N., and Knepper D.H. *Spectral plot program for accessing the USGS digital spectral library database with MS-DOS personal computers. USGS Open-file*. Denver, Colorado, Rep.,93: 593p. (1993).
36. Loughlin W. Principal component analysis for alteration mapping. *Photogramm. Eng. Remote Sens.*, **57**(9): 1163–1169 (1991).
37. Lowell J.D., and Guilbert J.M. Lateral and vertical alteration-mineralization zoning in porphyry ore deposits. *Econ. Geol.*, **65**(4): 373–408 (1970).
38. Mars J.C., and Rowan L.C. Regional mapping of phyllic and argillic altered rocks in the Zagros magmatic arc, Iran, using Advanced Spaceborne Thermal Emission and Reflection Radiometer (ASTER) data and logical operator algorithms. *Geosphere*, **2**(3): 161-186 (2006).
39. Matthew M. W., Adler-Golden S. M., Berk A., Richtsmeier S. C., Levine R. Y., Bernstein L. S., Acharya P. K., Anderson G. P., Felde G. W., Hoke M. P., Ratkowski A., Burke H.H., Kaiser R. D., and Miller D. P. Status of Atmospheric Correction Using a MODTRAN4-based Algorithm. In Proceedings of Algorithms for Multispectral, Hyperspectral, and Ultraspectral Imagery, *SPIE*, **4049**: 199-207 (2000).
40. Mehdizadeh Tehrani S., Fotoohi V., and Naaimi Ghasabian N. *Remote sensing investigation in Anar, Shahrebabak, Dehaj and Rafsanjan- I geological sheet (1: 100000 scale), Urumieh Dokhtar project.* Geological survey of Iran, open report, (1981).
41. NICICo. a. *The final exploratory report of Chahfiroozeh copper deposit*. National Iranian Copper Industries, Tehran, Internal report (in Farsi) (2009).
42. NICICo. b. *The final exploratory report of Iju copper deposit*. National Iranian Copper Industries, Tehran, Internal report (in Farsi) (2009).
43. Ranjbar H., and Honarmand M. Integration and analysis of airborne geophysical and ETM+ data for exploration of porphyry type deposits in the Central Iranian Volcanic Belt, using fuzzy classification. *Int. J. Remote Sens.*, **25**(21): 4729-4741 (2004).
44. Ranjbar H., and Honarmand M. Exploration for base metal mineralization in the southern part of the Central Iranian Volcanic Belt by using ASTER and ETM+ data. *J. Eng. Sci.*, **3**: 23-34 (2007).
45. Rowan L.C., Hook S.J., Abrams M.J., and Mars J.C. Mapping hydrothermally altered rocks at Cuprite, Nevada, using the advanced space borne thermal emission and reflection radiometer (Aster), a new satellite-imaging system. *Econ. Geol.*, **98**: 1018-1027 (2003).
46. Rowan L.C., and Mars J.C. Lithologic mapping in the Mountain Pass, California, area using Advanced Spaceborne Thermal Emission and Reflection Radiometer (ASTER) data. *Remote Sens. Environ.*, **84**(3): 350–366 (2003).
47. Rowan L.C., Schmidt R.G., and Mars J.C. Distribution of hydrothermally altered rocks in the Reko Diq, Pakistan mineralized area based on spectral analysis of ASTER data. *Remote Sens. Environ.*, **104**(1): 74–87 (2006).
48. Ruiz-Armenta J.R., and Prol-Ledesma R.M. Techniques for enhancing the spectral response of hydrothermal alteration minerals in Thematic Mapper images of central Mexico. *Int. J. Remote Sens.*, **19**(10): 1981–2000 (1998).
49. Sabins F.F. Remote sensing for mineral exploration. *Ore Geol. Rev.*, **14**(3): 157-183 (1999).
50. Saric V., and Mijalkovic N. *Metallogenic map of Kerman region, 1:500000 scale. In: Exploration for ore deposits in Kerman region*. Geological Survey of Iran publication, Tehran, Rep., 53, 247p. (1973).
51. Shafiei B., Haschke M., and Shahabpour J. Recycling of orogenic arc crust triggers porphyry Cu mineralization in Kerman Cenozoic arc rocks, southeastern Iran. *Mineral. Deposita*, **44**(3): 265-283 (2009).
52. Shahabpour J. Aspects of Alteration and Mineralization at the Sar-Cheshmeh Copper–Molybdenum Deposit, Kerman, Iran. Unpublished PhD *Thesis*, University of Leeds, England, 342 p. (1982).
53. Tangestani M.H., and Moore F. Comparison of three principal component analysis techniques to porphyry copper alteration mapping a case study in Meiduk area, Kerman, Iran. *Can. J. Remote Sens.*, **27**(2): 176–182 (2001).
54. Tangestani M.H., Mazhari N., Agar B., and Moore F. Evaluating Advanced Spaceborne Thermal Emission and Reflection Radiometer (ASTER) data for alteration zone enhancement in a semi arid area, northern Shahr-e-Babak, SE Iran. *Int. J. Remote Sens.*, **29**(10): 2833-2850 (2008).
55. Tommaso I.D., and Rubinstein N. Hydrothermal alteration mapping using ASTER data in the Infiernillo porphyry deposit, Argentina. *Ore Geol. Rev.*, **32**(1-2): 275-290 (2007).
56. Waterman G.C., and Hamilton R.L. The Sar-Cheshmeh porphyry copper deposit. *Econ. Geol.* **70**(3): 568–576 (1975).
57. Zarasvandi A., Liaghat S., and Zentilli M. Geology of the Darreh–Zerreshk and Ali-Abad porphyry copper deposits, Central Iran. *Int. Geol. Rev.*, **47**(6): 620–646 (2005).
58. Zhang X., Pazner M., and Duke N. Lithologic and mineral information extraction for gold exploration using ASTER data in the south Chocolate Mountains (California). *ISPRS J. Photogramm. Remote Sens.*, **62**(4): 271-282 (2007).